Global Kinetic Simulations of Monster Shocks and Their Emission

Dominic Bernardi,* Yajie Yuan,† and Alexander Y. Chen‡
Physics Department and McDonnell Center for the Space Sciences,
Washington University in St. Louis, St. Louis, Missouri, 63130, USA

(Received 4 June 2025; accepted 1 December 2025; published 22 December 2025)

Fast magnetosonic waves are one of the two low-frequency plasma modes that can exist in a neutron star magnetosphere. It was recently realized that these waves may become nonlinear within the magnetosphere and steepen into some of the strongest shocks in the universe. These shocks, when in the appropriate parameter regime, may emit GHz radiation in the form of precursor waves. We present the first global particle-in-cell simulations of the nonlinear steepening of fast magnetosonic waves in a dipolar magnetosphere, and quantitatively demonstrate the strong plasma acceleration in the upstream of these shocks. In these simulations, we observe the production of precursor waves in a finite angular range. Using analytic scaling relations, we predict the expected frequency, power, and duration of this emission. Within a reasonable range of progenitor wave parameters, these precursor waves can reproduce many aspects of FRB observations.

DOI: 10.1103/y9p7-1zms

Introduction—Magnetars are a class of young neutron stars with superstrong magnetic field, which can reach 10^{15} G on the stellar surface [1,2] (we use cgs units throughout this Letter). The evolution of the strong internal field is believed to induce starquakes or crustal displacements that twist up the external field, injecting energy into the magnetosphere, which eventually powers the prolific x-ray activities we observe from these objects [3]. Magnetars may also be promising progenitors of fast radio bursts (FRBs)—mysterious, millisecond duration radio bursts of cosmological origin. In fact, a simultaneous x-ray and radio burst was observed from the galactic magnetar SGR $1935+2154$ [4,5], corroborating this connection. However, a detailed physical mechanism for such simultaneous emission is still under debate.

Extensive analytic and numerical work has demonstrated that dynamic activity around magnetars will inevitably produce energetic fast magnetosonic waves. These waves can be launched either directly at the stellar surface through starquakes [6–10], or further out in the magnetosphere through mode conversion [11–14]. They can also be generated during cataclysmic stellar collapse [15], or a merger event [16].

*Contact author: bdominic@wustl.edu
†Contact author: yajiey@wustl.edu
‡Contact author: cyuran@wustl.edu

A fast wave emitted from near the neutron star expands spherically, and its amplitude decreases with radius as $\delta B \propto 1/r$. However, the background dipole magnetic field follows $B_{\rm bg} \propto 1/r^3$; therefore, $\delta B/B_{\rm bg} \propto r^2$—the relative amplitude grows with radius. If the wave amplitude is large enough, $\delta B/B_{\rm bg}$ may become order unity within the magnetosphere. In the high magnetization limit, the polarization of fast waves is such that the wave magnetic field $\delta\mathbf{B}$ is in the plane containing the wave vector $\mathbf{k}$ and the background magnetic field $\mathbf{B}_{\rm bg}$, while the wave electric field $\delta\mathbf{E}$ is perpendicular to this plane. Such a polarization implies that when $\delta B/B_{\rm bg}$ approaches unity, the wave magnetic field may cancel with the background magnetic field, potentially leading to macroscopic $E > B$ regions. In the MHD limit, such regions are not permitted, and the wave deforms to prevent $E > B$, converting a significant fraction of the wave energy into plasma bulk motion and forming a shock at every wavelength [8,17,18]. These shocks are named "monster shocks" by [8] due to the enormous Lorentz factor the upstream flow can reach. Recently, one dimensional kinetic simulations by [19] showed that these monster shocks can emit coherent precursor waves through the synchrotron maser instability, producing GHz signals that may resemble observed FRBs.

So far, existing studies of this monster shock have focused on the special case of the shock propagating perpendicularly to the magnetic field, which is only applicable on the equatorial plane of the magnetosphere. However, the nature of the shock and the observational consequences depend on the global geometry and field scaling. This type of problem is well suited for global multidimensional particle-in-cell (PIC) simulations, as demonstrated by numerous works in the past decade,

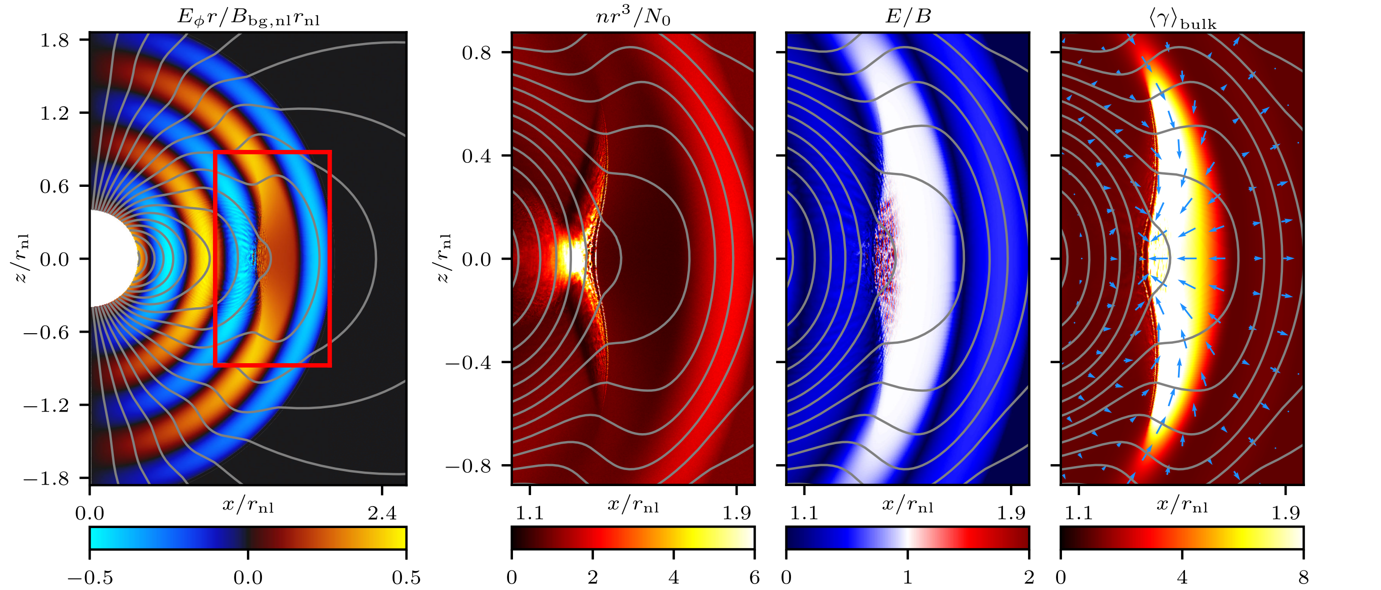

FIG. 1. Global structure of the monster shock from our fiducial simulation with fast wave wavelength $\lambda = 0.6r_{\rm nl}$ and $\sigma_{\rm bg,nl} = 250$. The snapshot is taken at time $t = 1.6r_{\rm nl}/c$. The left panel shows $E_\phi r/B_{\rm bg,nl}r_{\rm nl}$, where $B_{\rm bg,nl}$ is the equatorial magnetic field at the nonlinear radius. The subsequent three panels show a zoomed-in view of the region within the red box in the left panel, with colors representing the scaled plasma density nr^3/N_0 (where $N_0 = n_{\rm bg}r^3$ is a constant), the ratio of the electric field to the magnetic field, and the Lorentz factor of the bulk flow, respectively. In all panels the gray lines are the magnetic field lines. In the rightmost panel, the blue arrows indicate the direction of the bulk flow, and the arrow lengths are proportional to the bulk velocity [36].

e.g., [20–23]. In this Letter, we present the first 2D global PIC simulations of the monster shock formation due to nonlinear evolution of fast waves in a dipolar magnetosphere. For the first time, we demonstrate the scaling of the upstream Lorentz factor and its evolution in kinetic simulations with realistic geometry. We also show the self-consistent structure of the shock globally, and quantify how this structure affects the precursor wave production. Finally we estimate the properties of the resulting precursor waves and compare with the properties of observed FRBs.

Simulation parameters—Consider a magnetar with surface magnetic field $B_* = B_{15}10^{15}$ G and stellar radius $r_* \sim 10^6$ cm, producing x-ray bursts with a typical luminosity $L = L_{42}10^{42}$ erg s^{-1}. Assuming an x-ray burst is produced from a fast wave with comparable luminosity, this wave will become nonlinear when $\delta B/B_{\rm bg} \sim 1/2$, at a radius

$$r_{\rm nl} = \sqrt{\frac{B_* r_*^3}{2}}\left(\frac{L}{c}\right)^{-1/4} \approx 2.9 \times 10^8 B_{15}^{1/2} L_{42}^{-1/4}\ \text{cm}. \quad (1)$$

This is the central length scale of our problem. As a comparison, the light cylinder, where the magnetic field has to open up otherwise the plasma corotating with the neutron star would reach the speed of the light, is located at $r_{\rm LC} = cP/(2\pi) \sim 4.8 \times 10^9 P_0$ cm, where $P = P_0 1$ s is the spin period of the neutron star. In fact, as long as $L \gtrsim 1.4 \times 10^{37} P_0^{-4} B_{15}^2$ erg s^{-1}, the fast wave can become nonlinear within the light cylinder.

Our simulations are performed in 2D spherical coordinates (r, θ) assuming axisymmetry, using our PIC code Aperture [24]. To capture the shock physics, the simulations need to resolve both the plasma skin depth $\lambda_p = c/\omega_p = \sqrt{m_e c^2/(4\pi n_{\rm bg} e^2)}$ and the gyration timescale $\omega_B^{-1} = m_e c/(eB_{\rm bg})$ at the nonlinear radius. The ratio of these two scales is the magnetization, which is a key parameter of this problem:

$$\sigma_{\rm bg,nl} = \frac{B_{\rm bg}^2}{4\pi n_{\rm bg} m_e c^2} = \left(\frac{\omega_B}{\omega_p}\right)^2. \quad (2)$$

We have performed simulations with $\sigma_{\rm bg,nl}$ ranging from 160 to 2560, and fast wave wavelengths λ from $0.2r_{\rm nl}$ to $r_{\rm nl}$. To capture the kinetic scale of the shock, we ensure at least 4 cells per skin depth at the nonlinear radius in all our simulations. A detailed description of the simulation setup can be found in Supplemental Material [25].

Results—Across a wide range of simulation parameters, we observe the formation of the monster shock near the nonlinear radius $r_{\rm nl}$. We are able to verify the condition of shock formation predicted by [18] (see Supplemental Material [25] for quantitative discussion and demonstration). Figure 1 shows the global structure of the monster shock in our fiducial simulation with wavelength

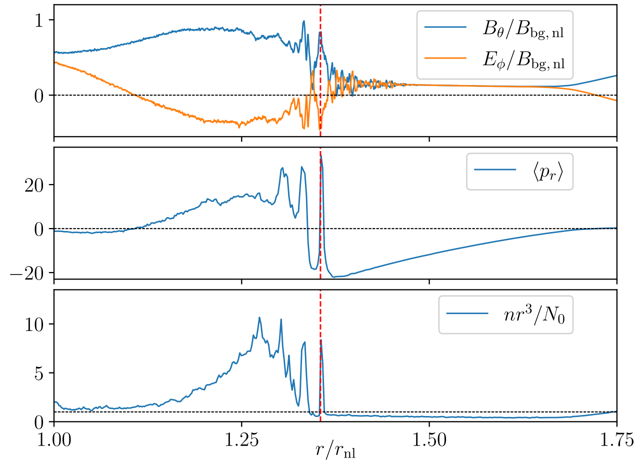

FIG. 2. Structure of the shock on the equatorial plane in our fiducial simulation at the same time as in Fig. 1. The top panel shows $B_\theta/B_{\mathrm{bg,nl}}$ and $E_\phi/B_{\mathrm{bg,nl}}$. The middle panel shows the radial component of the average plasma momentum $\langle p_r \rangle$. The third panel shows the scaled plasma density nr^3/N_0 and the horizontal dashed line indicates the value of N_0. The red dashed line marks the location of the shock.

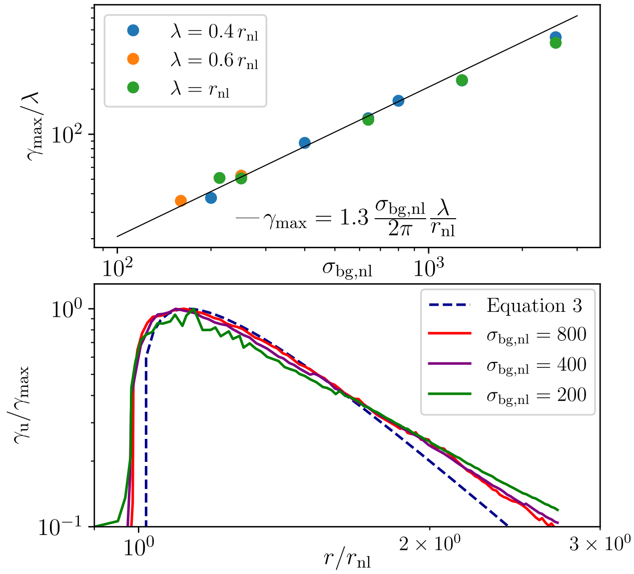

FIG. 3. The top panel shows the scaling of the maximum upstream Lorentz factor $\gamma_{\max}$ on the equatorial plane with the background magnetization at the nonlinear radius $\sigma_{\mathrm{bg,nl}}$. We divide the measured $\gamma_{\max}$ by the fast wave wavelength λ. The resulting scaling relation is linear: $\gamma_{\max}/\lambda \propto \sigma_{\mathrm{bg,nl}}$. The bottom panel shows γ_u as a function of position for simulations with different values of $\sigma_{\mathrm{bg,nl}}$, as well as the theoretically predicted curve [Eq. (3)]. For better comparison purposes, the curves are normalized by their own maximum value $\gamma_{\max}$.

$\lambda = 0.6 r_{\mathrm{nl}}$, $\sigma_{\mathrm{bg,nl}} = 250$, and $\lambda_p \approx 1.6 \times 10^{-3} r_{\mathrm{nl}}$ at the nonlinear radius. As the wave propagates beyond the nonlinear radius, the wave trough, in which $\delta B_\theta < 0$, significantly reduces the total magnetic field, because it partially cancels the background magnetic field. This first happens on the equator, then expands to higher latitudes as the fast wave propagates to larger radii. In this region (highlighted as a red box in the first panel of Fig. 1), the wave profile is significantly deformed to avoid $E > B$. As a result, a shock forms at the left edge of this region. In the upstream of this shock, the plasma bulk motion is accelerated in the $\mathbf{E} \times \mathbf{B}$ direction, reaching high Lorentz factors.

To see features of the shock more clearly, Fig. 2 shows a one-dimensional slice along the equator in the same fiducial simulation as in Fig. 1, taken at the same simulation time. The wave trough, as shown in B_θ, is significantly deformed and flattened out. In this region, $E \approx B \approx B_{\mathrm{bg}}/2$, and the bulk flow accelerates almost linearly towards the $-\hat{r}$ direction, reaching a Lorentz factor of more than 20. Because the plasma is frozen into the magnetic field, the density also drops to half the background value [8]. On the equatorial plane, the total magnetic field (in the $\hat{\theta}$ direction) is perpendicular to the bulk flow direction and the shock normal (both in the $\hat{r}$ direction); the resulting shock is a so-called perpendicular shock. In the shock transition region, two prominent solitons can be seen in all panels of Fig. 2 at $r = 1.35 r_{\mathrm{nl}}$ and $1.33 r_{\mathrm{nl}}$ and as the striped feature extending to higher latitudes in the density panel of Fig. 1. The center of the leading soliton is indicated by the red dashed line in Fig. 2 and conventionally marks the shock front. Such solitons are characteristic of quasiperpendicular collisionless shocks [37,38]. The cavity formed by the two solitons produce precursor waves that are transmitted into the upstream [39,40], shown as the fluctuations with $E > B$ both in the top panel of Fig. 2 and the third panel of Fig. 1. To the left of the solitons, the plasma goes through further phase space mixing, heats up, and transitions into the downstream flow. We have checked that the shock jump condition is consistent with MHD theory in the no-cooling regime.

In an analytic calculation of monster shocks in the MHD framework, [8] demonstrated that the plasma will be linearly accelerated to bulk Lorentz factors proportional to the background magnetization and the fast wave wavelength. On the equatorial plane, the bulk Lorentz factor will evolve as a function of position:

$$\gamma_u \approx \frac{\sigma_{\mathrm{bg,nl}}}{2\pi}\frac{\lambda}{r_{\mathrm{nl}}}\left(\frac{r_{\mathrm{nl}}}{r}\right)^4\left(\pi - 2\arcsin\left(\frac{r_{\mathrm{nl}}}{r}\right)^2\right). \quad (3)$$

γ_u attains a maximum value of $\gamma_{\max} \approx 0.81 \sigma_{\mathrm{bg,nl}} \lambda/(2\pi r_{\mathrm{nl}})$, at $r \approx 1.15 r_{\mathrm{nl}}$.

To test whether the kinetic shock obeys the MHD scaling relation and evolution, we perform a series of simulations with varying $\sigma_{\mathrm{bg,nl}}$ and λ. We measure γ_u upstream of the shock where the linear acceleration zone ends, and record

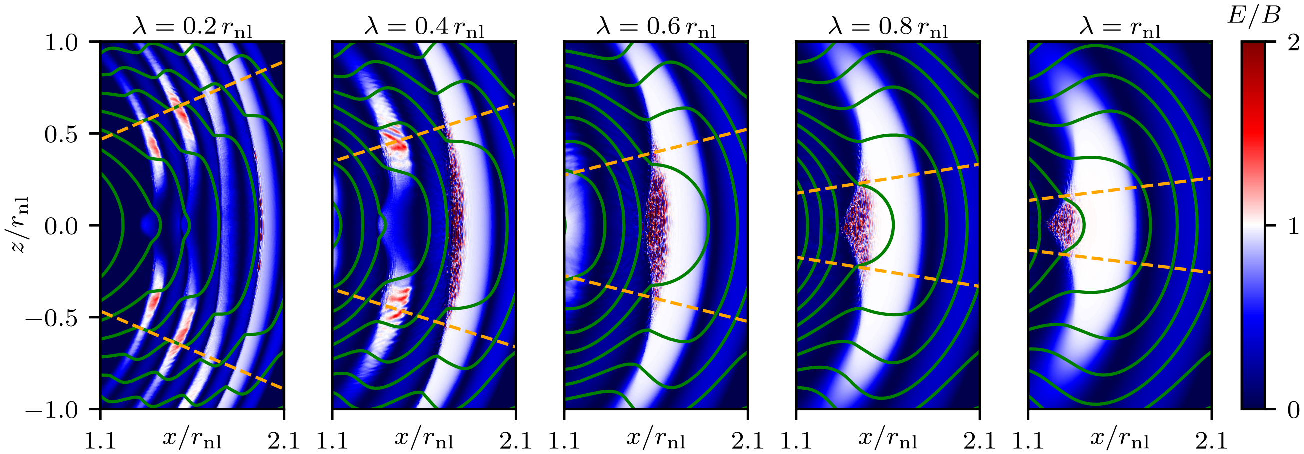

FIG. 4. The ratio of the total electric field to the total magnetic field for simulations with several different wavelengths. The fluctuating region with $E > B$ that occurs in the first full period of the fast wave is the precursor wave. The orange dashed lines mark the latitudes where the shock becomes parallel, namely, the magnetic field is parallel to the shock normal. From left to right, these latitudes are ±23°, ±18°, ±14°, ±9°, and ±7°, respectively. Subsequent shocks become modified due to heating of the plasma from the first shock, and $E > B$ regions show up at higher latitudes due to plasma flowing towards the equator. The snapshots are all taken at the same time $t = 2r_{\rm nl}/c$.

the maximum value γ_u attains over the history as $\gamma_{\rm max}$. The top panel of Fig. 3 shows that $\gamma_{\rm max}/\lambda$ depends linearly on $\sigma_{\rm bg,nl}$, as predicted by MHD. However, we measured a slightly larger prefactor, so the resulting scaling relation is

$$\gamma_{\rm max} \approx 1.3 \frac{\sigma_{\rm bg,nl}}{2\pi}\left(\frac{\lambda}{r_{\rm nl}}\right). \tag{4}$$

In other words, the bulk acceleration is even more efficient than predicted by [8]. The bottom panel of Fig. 3 shows γ_u as a function of position for three different simulations, normalized by their own maximum value. We see that the evolution of γ_u in our simulations agrees well with the theoretical prediction, especially during early stages of the shock propagation. At late stages, the measured γ_u decreases with r slower than the theoretical prediction, closer to $1/r^3$. This may depend on the background magnetization $\sigma_{\rm bg,nl}$, as Eq. (3) was derived for extremely high $\sigma_{\rm bg,nl}$.

Away from the equatorial plane, the plasma flow is no longer perpendicular to the shock. The upstream velocity is dominated by the $\mathbf{E} \times \mathbf{B}$ drift, which develops an increasing $\hat{\theta}$ component at higher latitudes, as shown in the rightmost panel of Fig. 1. Therefore, the upstream flow at high latitudes is oblique with respect to the shock normal. Interestingly, our simulations demonstrate that the scaling of the maximum upstream Lorentz factor still depends linearly on the background magnetization. This flow also directs plasma from higher latitudes towards the equator, increasing the density in the equatorial plane while decreasing the density at higher latitudes. Consequently the density at high latitudes may decrease enough to no longer prevent $E > B$ in subsequent shocks (see discussion in Supplemental Material [25]).

Another important factor that determines the shock properties is the magnetic obliquity, defined as the angle between the magnetic field and the shock normal in the *upstream* rest frame [41]. The orientation of the magnetic field with respect to the shock generally depends on the reference frame. However, when the magnetic field is parallel to the shock normal, an arbitrary Lorentz transformation does not change this angle, therefore we can directly identify a parallel shock in our simulation frame. For all of our simulations, we do see that the shock becomes parallel at sufficiently high latitudes. We measured the latitudes $\pm\ell_\parallel$ where the shock becomes parallel, and found that the value does not evolve much over time after the shock has formed; it has a strong dependence only on the fast wave wavelength λ. The results are shown in Fig. 4. We found that within the equatorial region bounded by the critical latitudes $\pm\ell_\parallel$, the upstream drifts inward toward the shock; at higher latitudes beyond $\pm\ell_\parallel$, the upstream drifts outward and the shock is catching up with the upstream flow instead.

Figure 4 also shows that the shape of the shock front depends on the fast wave wavelength λ. The shock front can be visualized as the region separating the upstream, where $E \approx B$ from the downstream, where $E/B < 1$. When $\lambda \ll r_{\rm nl}$, the shock front is approximately spherical. However, as λ approaches $r_{\rm nl}$, the shock front gets deformed from a spherical shape: the equatorial section lags behind the segments at higher latitudes. The effect is most extreme for the run with $\lambda = r_{\rm nl}$. We discuss the reason behind this in the End Matter.

As an important feature of magnetized shocks, the formation of precursor waves is dependent on the magnetic obliquity. Figure 4 shows that the region with precursor wave production is around the equator, roughly bounded by the latitudes where the shock becomes parallel. This suggests that precursor waves are most efficiently produced at quasi-perpendicular shocks, when the upstream is accelerated towards the shock. They are suppressed when the shock becomes parallel. We further discuss a few kinematic considerations that affect the appearance of the precursor waves in the End Matter.

Astrophysical implications—Our global kinetic simulations have shown that the monster shock can indeed emit a coherent precursor wave, and this may be a promising mechanism for FRBs [19]. For a typical fast wave of luminosity $L = L_{42}10^{42}$ erg s^{-1} and frequency $\omega = \omega_4 10^4$ rad s^{-1} launched from a magnetar of surface magnetic field $B_* = B_{15}10^{15}$ G, we estimate the peak frequency of the radio emission when the shock has just formed beyond the nonlinear radius to be $\nu_{\rm peak}(r_{\rm nl}) \sim 0.22 B_{15}^{1/2} L_{42}^{-1/4} M_6 P_0^{-1} \omega_4$ GHz, and the peak luminosity of the radio waves is $L_R(r_{\rm nl}) \sim 5.4\times 10^{37} B_{15}^{-1/2} L_{42}^{3/4} \omega_4^{-1}$ erg s^{-1} (see the End Matter for the detailed calculations). Afterward, $\nu_{\rm peak}(r)$ increases with r linearly, but the luminosity quickly decreases with radius as $L_R \propto r^{-5}$, so most of the radio emission is produced between $r_{\rm nl} < r < 3r_{\rm nl}$. The duration of the observed radio emission is $\Delta t_{\rm obs} \sim 0.5\omega_4^{-1}$ ms if we only consider the first shock, but the subsequent shocks could continue to emit and produce substructures in the observed bursts similar to those seen in some FRBs [42]. We thus conclude that with appropriate parameters, the monster shock is promising to produce observed FRBs, especially the one from the Galactic magnetar SGR $1935 + 2154$. The shock will also produce a multiwavelength counterpart from incoherent radiation in the downstream. This emission is discussed in the End Matter.

Conclusion—We have carried out the first 2D global PIC simulations of monster shock formation due to nonlinear steepening of fast waves in neutron star magnetospheres. We confirmed efficient conversion of electromagnetic energy into plasma kinetic energy: the maximum upstream Lorentz factor is indeed linearly proportional to the background magnetization and the fast wave wavelength. We observed the production of precursor waves from the monster shock and measured its angular range. We found that with typical magnetar parameters, the monster shock can be a promising mechanism for some FRBs, especially the ones from the Galactic magnetar SGR $1935 + 2154$. However, more study is needed to investigate whether these radio waves can escape from the magnetosphere. We are also in need of a systematic study of precursor waves emitted from shocks of general magnetic obliquity to obtain more precise predictions of the radio spectra and polarization away from the magnetic equator.

Acknowledgments—We thank Andrei Beloborodov, Michael Grehan, Amir Levinson, Yuanhong Qu, Andrew Sullivan, and Arno Vanthieghem for helpful discussions. A. C. and Y. Y. acknowledge support from NSF Grants No. DMS-2235457 and No. AST-2308111 as well as from NASA Grant No. 80NSSC25K0080. A. C. also acknowledges support from NASA Grant No. 80NSSC24K1095. This work was also facilitated by the Multimessenger Plasma Physics Center (MPPC), NSF Grant No. PHY-2206608, and by a grant from the Simons Foundation (MP-SCMPS-00001470) to Y. Y. This research used resources of the Oak Ridge Leadership Computing Facility at the Oak Ridge National Laboratory, which is supported by the Office of Science of the U.S. Department of Energy under Contract No. DE-AC05-00OR22725. The authors also acknowledge the Research Infrastructure Services (RIS) group at Washington University in St. Louis for providing computational resources and services that were used to generate parts of the research results delivered within this paper. We thank the hospitality of the Kavli Institute for Theoretical Physics (KITP), where we had fruitful discussions with colleagues as we revised the manuscript. This research was supported in part by Grant No. NSF PHY-2309135 to the KITP.

Data availability—The data that support the findings of this article are not publicly available upon publication because it is not technically feasible and/or the cost of preparing, depositing, and hosting the data would be prohibitive within the terms of this research project. The data are available from the authors upon reasonable request.

[1] V. M. Kaspi and A. M. Beloborodov, Magnetars, Annu. Rev. Astron. Astrophys. **55**, 261 (2017).

[2] S. Mereghetti, J. A. Pons, and A. Melatos, Magnetars: Properties, origin and evolution, Space Sci. Rev. **191**, 315 (2015).

[3] C. Thompson and R. C. Duncan, The soft gamma repeaters as very strongly magnetized neutron stars. II. Quiescent neutrino, x-ray, and Alfven wave emission, Astrophys. J. **473**, 322 (1996).

[4] B. C. Andersen *et al.* (CHIME/FRB Collaboration), A bright millisecond-duration radio burst from a Galactic magnetar, Nature (London) **587**, 54 (2020).

[5] C. D. Bochenek, V. Ravi, K. V. Belov, G. Hallinan, J. Kocz, S. R. Kulkarni, and D. L. McKenna, A fast radio burst associated with a Galactic magnetar, Nature (London) **587**, 59 (2020).

[6] O. Blaes, R. Blandford, P. Goldreich, and P. Madau, Neutron starquake models for gamma-ray bursts, Astrophys. J. **343**, 839 (1989).

[7] A. Bransgrove, A. M. Beloborodov, and Y. Levin, A quake quenching the vela pulsar, Astrophys. J. **897**, 173 (2020).

[8] A. M. Beloborodov, Monster radiative shocks in the perturbed magnetospheres of neutron stars, Astrophys. J. **959**, 34 (2023).

[9] Y. Qu and A. Bransgrove, Three-dimensional numerical simulations of magnetar crust quakes, arXiv:2508.12567.

[10] L. Burnaz, E. R. Most, and A. Bransgrove, Crustal quakes spark magnetospheric blasts: Imprints of realistic magnetar

crust oscillations on the fast radio burst signal, arXiv: 2508.18033.

[11] Y. Yuan, Y. Levin, A. Bransgrove, and A. Philippov, Alfvén wave mode conversion in pulsar magnetospheres, Astrophys. J. **908**, 176 (2021).

[12] J. F. Mahlmann, M. Á. Aloy, and X. Li, Force-free wave interaction in magnetar magnetospheres: Computational modeling in axisymmetry, Astrophys. J. **972**, 139 (2024).

[13] D. Bernardi, Y. Yuan, and A. Y. Chen, Alfvén wave conversion to low frequency fast magnetosonic waves in magnetar magnetospheres, Astrophys. J. **980**, 222 (2025).

[14] A. Y. Chen, Y. Yuan, and D. Bernardi, Alfvén wave mode conversion in neutron star magnetospheres: A semianalytic approach, Astrophys. J. **987**, 42 (2025).

[15] E. R. Most, A. M. Beloborodov, and B. Ripperda, Monster shocks, gamma-ray bursts, and black hole quasi-normal modes from neutron-star collapse, Astrophys. J. Lett. **974**, L12 (2024).

[16] Y. Kim, E. R. Most, A. M. Beloborodov, and B. Ripperda, Black hole pulsars and monster shocks as outcomes of black hole–neutron star mergers, Astrophys. J. Lett. **982**, L54 (2025).

[17] Y. E. Lyubarsky, Fast magnetosonic waves in pulsar winds, Mon. Not. R. Astron. Soc. **339**, 765 (2003).

[18] A. Y. Chen, Y. Yuan, X. Li, and J. F. Mahlmann, Propagation of a strong fast magnetosonic wave in the magnetosphere of a neutron star, arXiv:2210.13506.

[19] A. Vanthieghem and A. Levinson, Fast radio bursts as precursor radio emission from monster shocks, Phys. Rev. Lett. **134**, 035201 (2025).

[20] A. Y. Chen and A. M. Beloborodov, Electrodynamics of axisymmetric pulsar magnetosphere with electron-positron discharge: A numerical experiment, Astrophys. J. Lett. **795**, L22 (2014).

[21] A. A. Philippov and A. Spitkovsky, *Ab-initio* pulsar magnetosphere: Particle acceleration in oblique rotators and high-energy emission modeling, Astrophys. J. **855**, 94 (2018).

[22] B. Cerutti and G. Giacinti, A global model of particle acceleration at pulsar wind termination shocks, Astron. Astrophys. **642**, A123 (2020).

[23] A. G. Sullivan, J. Cortés, and L. Sironi, Polarized emission of intrabinary shocks in spider pulsars from global 3D kinetic simulations, Astrophys. J. **991**, 98 (2025).

[24] https://github.com/fizban007/Aperture4.

[25] See Supplemental Material at http://link.aps.org/supplemental/10.1103/y9p7-1zms for additional discussion which includes Refs. [26–35].

[26] J. L. Vay, Simulation of beams or plasmas crossing at relativistic velocity, Phys. Plasmas **15**, 056701 (2008).

[27] T. Z. Esirkepov, Exact charge conservation scheme for particle-in-cell simulation with an arbitrary form-factor, Comput. Phys. Commun. **135**, 144 (2001).

[28] A. Y. Chen, M. Luepker, and Y. Yuan, Introducing Aperture: A GPU-based general relativistic particle-in-cell simulation framework, arXiv:2503.04558.

[29] B. Cerutti, A. Philippov, K. Parfrey, and A. Spitkovsky, Particle acceleration in axisymmetric pulsar current sheets, Mon. Not. R. Astron. Soc. **448**, 606 (2015).

[30] A. Y. Chen, Particle-in-cell simulations and their applications to magnetospheres of neutron stars, Ph.D. thesis, Columbia University, 2017.

[31] A. Y. Chen, F. Cruz, and A. Spitkovsky, Filling the magnetospheres of weak pulsars, Astrophys. J. **889**, 69 (2020).

[32] A. Y. Chen and A. M. Beloborodov, Particle-in-cell simulations of the twisted magnetospheres of magnetars. I, Astrophys. J. **844**, 133 (2017).

[33] J. D. Jackson, Classical electrodynamics, 3rd ed. (Wiley, New York, NY, 1999).

[34] Y. Yuan, A. M. Beloborodov, A. Y. Chen, Y. Levin, E. R. Most, and A. A. Philippov, Magnetar bursts due to Alfvén wave nonlinear breakout, Astrophys. J. **933**, 174 (2022).

[35] Y. Zhang, Y. Yang, and L. Ji, Radiation reaction effects on coherent emission in relativistic magnetized shocks, arXiv:2502.14550.

[36] Click here (https://youtu.be/LyQCaSag0Zc) for a YouTube video of these shocks.

[37] D. Alsop and J. Arons, Relativistic magnetosonic solitons with reflected particles in electron-positron plasmas, Phys. Fluids **31**, 839 (1988).

[38] A. Vanthieghem and A. Levinson, Relativistically magnetized collisionless shocks in pair plasma: Solitons, chaos, and thermalization, Phys. Rev. E **111**, 045209 (2025).

[39] Y. A. Gallant, M. Hoshino, A. B. Langdon, J. Arons, and C. E. Max, Relativistic, perpendicular shocks in electron-positron plasmas, Astrophys. J. **391**, 73 (1992).

[40] I. Plotnikov and L. Sironi, The synchrotron maser emission from relativistic shocks in fast radio bursts: 1D PIC simulations of cold pair plasmas, Mon. Not. R. Astron. Soc. **485**, 3816 (2019).

[41] L. Sironi and A. Spitkovsky, Particle acceleration in relativistic magnetized collisionless pair shocks: Dependence of shock acceleration on magnetic obliquity, Astrophys. J. **698**, 1523 (2009).

[42] W. A. Majid, A. B. Pearlman, T. A. Prince, R. S. Wharton, C. J. Naudet, K. Bansal, L. Connor, M. Bhardwaj, and S. P. Tendulkar, A bright fast radio burst from FRB 20200120E with sub-100 nanosecond structure, Astrophys. J. Lett. **919**, L6 (2021).

[43] P. Goldreich and W. H. Julian, Pulsar electrodynamics, Astrophys. J. **157**, 869 (1969).

[44] S. Mereghetti *et al.*, INTEGRAL discovery of a burst with associated radio emission from the magnetar SGR $1935+2154$, Astrophys. J. Lett. **898**, L29 (2020).

[45] A. Ridnaia, D. Svinkin, D. Frederiks, A. Bykov, S. Popov, R. Aptekar, S. Golenetskii, A. Lysenko, A. Tsvetkova, M. Ulanov, and T. L. Cline, A peculiar hard x-ray counterpart of a Galactic fast radio burst, Nat. Astron. **5**, 372 (2021).

[46] C. K. Li *et al.*, HXMT identification of a non-thermal x-ray burst from SGR J$1935+2154$ and with FRB 200428, Nat. Astron. **5**, 378 (2021).

[47] A.-N. Babul and L. Sironi, The synchrotron maser emission from relativistic magnetized shocks: dependence on the pre-shock temperature, Mon. Not. R. Astron. Soc. **499**, 2884 (2020).

[48] S. D. Ryder *et al.*, A luminous fast radio burst that probes the Universe at redshift 1, Science **382**, 294 (2023).

[49] C. Thompson and R. C. Duncan, The soft gamma repeaters as very strongly magnetized neutron stars—I. Radiative mechanism for outbursts, Mon. Not. R. Astron. Soc. **275**, 255 (1995).

End Matter

2D shock structure—We can understand the trend of the shock shape shown in Fig. 4 based on the following considerations. As has been shown by [8], the fast wave becomes nonlinear and forms a shock first on the equator. Then, the higher latitude portion of the wave forms a shock at larger radii. The shape of the shock front is then determined by both the location where it forms, as well as its speed. The latter depends on the local upstream magnetization. In our simulations, the upstream magnetization on the equator can be expressed using the lab-frame-measured magnetic field B and density n as $\sigma_u = B^2/(4\pi n\gamma m_e c^2)$. Just beyond the nonlinear radius, we have $B \sim B_{\rm bg}/2$, $n \sim n_{\rm bg}/2$, and $\gamma \sim \gamma_{\rm max} \sim 1.3(\sigma_{\rm bg,nl}/2\pi)(\lambda/r_{\rm nl})$ according to Eq. (4), so

$$\sigma_u \sim \frac{\sigma_{\rm bg,nl}}{2\gamma_{\rm max}} \sim \frac{\pi r_{\rm nl}}{1.3\lambda}. \tag{A1}$$

Interestingly, this does not depend on $\sigma_{\rm bg}$. It is known from MHD theory that when $\sigma_u \gg 1$, the shock Lorentz factor in the downstream frame is $\gamma_{\rm sh|d} \sim \sqrt{\sigma_u}$. In the lab frame, the plasma in the downstream is moving nonrelativistically, so the shock speed in the lab frame is $\gamma_{\rm sh} \sim \gamma_{\rm sh|d} \sim \sqrt{\sigma_u}$ when $\sigma_u \gg 1$. We can immediately see that $\gamma_{\rm sh}$ decreases with increasing fast wave wavelength λ. As λ approaches $r_{\rm nl}$, the upstream magnetization σ_u drops toward order unity, and the shock speed becomes significantly less than the speed of light. Therefore, the equatorial shock propagates slower than the unshocked wave at higher latitudes. When the latter also forms a shock at a larger radius, the equatorial shock is already lagging behind, producing the concave shock shape seen in the right panels of Fig. 4.

The reason why the shock becomes parallel at smaller latitudes as λ decreases is now twofold. First, the concave shock shape makes the shock normal point toward the equator at small latitudes. Second, the upstream plasma drifts toward the equator, bringing in the background magnetic field with it—an effect that becomes more prominent when the upstream magnetization is reduced and the plasma inertia becomes significant. In the other limit when $\lambda \ll r_{\rm nl}$, $\sigma_u \gg 1$ is satisfied and the shock propagates at a highly relativistic speed. The equatorial shock does not significantly lag behind the unshocked wave at higher latitudes, and the resulting shock surface approaches the spherical limit. In this case, the deformation of the upstream magnetic field due to plasma drift is also negligible; therefore, the shock becomes parallel when the upstream magnetic field is purely radial, at a polar angle of $\theta = \sin^{-1}(2/\sqrt{5}) \approx 63°$ [8], or a latitude of $\ell \approx 27°$. This is independent of the angular profile of the original fast wave.

There are a few kinematic considerations that affect the appearance of the precursor waves in this global setting. The precursor waves are likely emitted from the shock surface with a range of wave vector $\mathbf{k}$. However, only the waves emitted within an opening angle of $\sim 1/\gamma_{\rm sh}$ around the local shock normal may outrun the shock. For relatively slowly moving shocks at large fast wave wavelength λ, this opening angle can be of order unity, therefore the precursor waves may be able to extend beyond the $\ell_\parallel$ bound. In addition, the length of the precursor wave train in the lab frame depends on the Lorentz factor of the shock $\gamma_{\rm sh}$. If the duration of the precursor wave emission is Δt, then the wave train length in the lab frame is $\Delta l \sim c\Delta t/\gamma_{\rm sh}^2$ in the regime $\gamma_{\rm sh} \gg 1$. This is reflected in Fig. 4 as the precursor wave is barely visible in the $\lambda = 0.2 r_{\rm nl}$ case.

Application to astrophysical FRBs—We consider a fast wave with a luminosity of $L = L_{42} 10^{42}$ erg s^{-1}, to be consistent with typical magnetar x-ray bursts. Its frequency is determined by the underlying starquake, on the order of $\omega = \omega_4 10^4$ rad s^{-1} [6]. Suppose the magnetar has a surface magnetic field strength of $B_* = B_{15} 10^{15}$ G and a spin period of $P = P_0 1$ s. We estimate the plasma density at the stellar surface to be $n_* \approx \mathcal{M} n_{\rm GJ} \approx 6.9 \times 10^{19} B_{15} \mathcal{M}_6 P_0^{-1}$ cm^{-3} where $\mathcal{M} = \mathcal{M}_6 10^6$ is the pair multiplicity and $n_{\rm GJ} = B_*/ecP = 6.9 \times 10^{13} B_{15} P_0^{-1}$ cm^{-3} is the Goldreich Julian density [43] at the stellar surface. These parameters and Eq. (1) imply a nonlinear radius of $r_{\rm nl} \approx 2.9 \times 10^8 B_{15}^{1/2} L_{42}^{-1/4}$ cm and the ratio of the fast wave wavelength to the nonlinear radius is

$$\lambda/r_{\rm nl} \approx 6.5 \times 10^{-2} B_{15}^{-1/2} L_{42}^{1/4} \omega_4^{-1}. \tag{B1}$$

The background magnetization at the nonlinear radius is then

$$\sigma_{\rm bg,nl} \equiv \frac{B_{\rm bg,nl}^2}{4\pi n_{\rm bg,nl} m_e c^2} = 5.7 \times 10^7 B_{15}^{-1/2} L_{42}^{3/4} M_6^{-1} P_0. \tag{B2}$$

Using Eq. (4), the maximum value that the upstream Lorentz factor will attain is

$$\gamma_{\rm max} \sim 7.7 \times 10^5 B_{15}^{-1} L_{42} M_6^{-1} P_0 \omega_4^{-1}. \tag{B3}$$

This happens just slightly past the nonlinear radius where the shock first forms. The upstream magnetization is reduced to, according to Eq. (A1),

$$\sigma_{\rm u}(r_{\rm nl}) \approx \pi r_{\rm nl}/(1.3\lambda) \approx 37 B_{15}^{1/2} L_{42}^{-1/4} \omega_4. \tag{B4}$$

For definiteness, we estimate the properties of the expected radio emission at the magnetic equator, since the obliquity of the shock makes the prediction about precursor wave emission much more difficult elsewhere. According to [40], the low frequency cutoff of the precursor wave in the downstream frame is $\omega_{\mathrm{cutoff}} = \gamma_{\mathrm{sh|d}}\omega_p \approx \sqrt{\sigma_u}\omega_p$ and the peak frequency is $\omega_{\mathrm{peak}} \approx 3\omega_{\mathrm{cutoff}}$, where $\omega_p = \sqrt{4\pi n e^2/m_e\gamma}$ is the proper plasma frequency of the upstream measured in the downstream frame. When the shock first forms, the upstream Lorentz factor reaches its maximum, $\gamma \approx \gamma_{\max}$, the magnetic field, density, and magnetization reduce to half their background value. Combining these, the cutoff frequency immediately after the shock forms is $\omega_{\mathrm{cutoff}} \approx 4.7\times 10^8 B_{15}^{1/2} L_{42}^{-1/4} M_6 P_0^{-1}\omega_4\ \mathrm{rad\,s^{-1}}$. Therefore, the precursor wave spectrum will peak near

$$\nu_{\mathrm{peak}}(r_{\mathrm{nl}}) = \frac{\omega_{\mathrm{peak}}(r_{\mathrm{nl}})}{2\pi} \approx 0.22 B_{15}^{1/2} L_{42}^{-1/4} M_6 P_0^{-1}\omega_4\ \mathrm{GHz}. \tag{B5}$$

The precursor wave efficiency, defined as the fraction of the total incoming energy entering the shock that is channeled into the precursor waves, is $f \approx 2\times 10^{-3}/\sigma_u$ [40]. In our case, the precursor wave luminosity when the shock first forms just beyond r_{nl} is

$$L_R(r_{\mathrm{nl}}) \sim fL \sim 5.4\times 10^{37} B_{15}^{-1/2} L_{42}^{3/4}\omega_4^{-1}\ \mathrm{erg\,s^{-1}}. \tag{B6}$$

With appropriate parameters, the precursor wave frequency and luminosity can be consistent with observed FRBs, especially FRB 200428 from the galactic magnetar SGR 1935 + 2154. FRB 200428 was detected by CHIME, with an energy emitted in the 400–800-MHz band of 3×10^{34} erg and a peak luminosity of $7\times 10^{36}\ \mathrm{erg\,s^{-1}}$ [4]. It was also detected by STARE2 in the 1.281–1.468 GHz band, with an isotropic equivalent energy release of 2.2×10^{35} erg and a full-width at half-maximum (FWHM) temporal width of ∼0.6 ms, suggesting a luminosity $\sim 4\times 10^{38}\ \mathrm{erg\,s^{-1}}$ [5]. Since SGR 1935 + 2154 has a surface magnetic field of $B_{15}\sim 0.2$ and a period $P_0 \approx 3.2$, we can see that $\nu_{\mathrm{peak}}(r_{\mathrm{nl}})$ would be around 1.4 GHz if we take $M_6 \sim 45$, $\omega_4 \sim 1$ and $L_{42}\sim 1$; these parameters would give $L_R(r_{\mathrm{nl}}) \sim 10^{38}\ \mathrm{erg\,s^{-1}}$, consistent with observations obtained by CHIME and STARE2. FRB 200428 was also accompanied by an x-ray burst, with a duration of ∼0.6 s, superimposed by spikes coincident with the radio bursts. The energy released in the x-ray burst is $\sim 10^{40}\ \mathrm{erg\,s^{-1}}$, consistent with our choice of a fast wave luminosity of $L_{42}\sim 1$ [44–46].

As the shock propagates to larger radii, the upstream Lorentz factor evolves as $\gamma \sim \gamma_{\max}(r/r_{\mathrm{nl}})^{-4}$ according to Eq. (3), and the upstream magnetic field is kept at $B_{\mathrm{up}} = B_{\mathrm{bg}}/2 \propto r^{-3}$, while the density remains as $n = n_{\mathrm{bg}}/2 \propto r^{-3}$; therefore, the upstream magnetization evolves as $\sigma_u(r) \propto r$. The upstream proper plasma frequency evolves as $\omega_p \propto \sqrt{n/\gamma} \propto \sqrt{r}$. This results in the peak frequency of the precursor wave increasing with radius: $\omega_{\mathrm{peak}} \approx 3\sqrt{\sigma_u}\omega_p \propto r$. However, the luminosity of the precursor waves quickly drops with radius: the total incoming power entering the shock front is $L_u \sim r^2 c B_{\mathrm{up}}^2 \propto r^{-4}$; therefore, $L_R \sim fL_u \propto r^{-5}$. The luminosity of the precursor waves reduces to less than 0.5% of its peak value $L_R(r_{\mathrm{nl}})$ when the shock has propagated to a radius of $r = 3r_{\mathrm{nl}}$. All of the radio emission is effectively produced between $r_{\mathrm{nl}} < r < 3r_{\mathrm{nl}}$.

We also estimate the duration of the observed precursor wave emission. We take the duration of the emission as $\Delta t \sim 2r_{\mathrm{nl}}/c$, and the shock Lorentz factor is approximately $\gamma_{\mathrm{sh}} \sim \sqrt{\sigma_u(r_{\mathrm{nl}})}$ (a lower bound), so we get the observed duration $\Delta t_{\mathrm{obs}} \sim \Delta t/\gamma_{\mathrm{sh}}^2 \sim 0.5\omega_4^{-1}$ ms (an upper bound). This is shorter than typical FRBs. However, here we only considered the first shock launched in the first wavelength of the fast wave. The subsequent wavelengths of the fast wave can also launch shocks when they become nonlinear; the downstream of the previous shock will become the upstream of the next shock. Although the precursor wave emission can be suppressed when the upstream plasma is relativistically hot [47], if the cooling of the plasma is efficient (e.g., through incoherent synchrotron radiation), the subsequent shocks could have a sufficiently cold upstream that allows precursor wave emission. The total energetics and duration of the observed radio emission will then be determined by the full fast wave train, and the individual shocks may produce substructures in the observed bursts, on a timescale of $\delta t \sim \lambda/c \sim 0.6\omega_4^{-1}$ ms. This timescale may correspond to the observed substructure in some bursts [42]. Since our simulations do not include any cooling processes, we cannot properly model the behavior of subsequent shocks. We leave this to future studies.

The monster shock scenario may not be able to account for the very bright cosmological FRBs. For example, the bright FRB 20220610A has a luminosity $L_R \sim 10^{45}\ \mathrm{erg\,s^{-1}}$ [48]. This would require a fast wave with luminosity $L \sim 10^{48}\ \mathrm{erg\,s^{-1}}$, which would become nonlinear at a radius $r_{\mathrm{nl}} \sim 9.3\times 10^6$ cm. Such a level of energy release in the highly magnetic compact region close to the magnetar would lead to copious pair production and the plasma would quickly become an optically thick fireball, similar to the giant flares [49]. It is questionable whether any radio waves can be produced or escape from such an environment. Alternative explanations for these bright FRBs are still needed.

The monster shock can also produce incoherent radiation in other wavelengths. Immediately downstream of the shock, the energetic particles entering from the upstream start to gyrate in the compressed magnetic field and produce synchrotron/curvature radiation. If we adopt the naive synchrotron formula, we get the maximum photon energy $E_{\mathrm{syn}} = 3h\gamma_{\max}^2 eB_{\mathrm{bg}}/(4\pi m_e c) \sim 0.4B_{15}^{-5/2}L_{42}^{11/4}M_6^{-2}P_0^2\omega_4^{-2}$ TeV. Note that this energy is comparable to $\gamma_{\max} m_e c^2$, indicating that the synchrotron emission likely proceeds in the quantum regime, where the particle will quickly give most of its energy to one single photon. The gamma ray photons at this energy can already produce pairs through magnetic pair production, increasing the downstream plasma density. A more careful radiative transfer calculation is required to compute the detailed pair yield and the resulting x-ray spectrum, and will be deferred to a future work.